# Circumbinary Disk Evolution in the Presence of an Outer Companion Star

Rebecca G. Martin[1,2] , Stephen Lepp[1,2] , Stephen H. Lubow[3] , Matthew A. Kenworthy[4] , Grant M. Kennedy[5], and David Vallet[6]

[1] Nevada Center for Astrophysics, University of Nevada, Las Vegas, 4505 South Maryland Parkway, Las Vegas, NV 89154, USA
[2] Department of Physics and Astronomy, University of Nevada, Las Vegas, 4505 South Maryland Parkway, Las Vegas, NV 89154, USA
[3] Space Telescope Science Institute, 3700 San Martin Drive, Baltimore, MD 21218, USA
[4] Leiden Observatory, University of Leiden, PO Box 9513, 2300 RA Leiden, The Netherlands
[5] Department of Physics and Centre for Exoplanets and Habitability, University of Warwick, Gibbet Hill Road, Coventry CV4 7AL, UK
[6] Department of Mechanical Engineering, University of Nevada, Las Vegas, 4505 South Maryland Parkway, Las Vegas, NV 89154, USA

## Abstract

We consider a hierarchical triple system consisting of an inner eccentric binary with an outer companion. A highly misaligned circumbinary disk around the inner binary is subject to two competing effects: (i) nodal precession about the inner binary eccentricity vector that leads to an increase in misalignment (polar alignment) and (ii) Kozai–Lidov (KL) oscillations of eccentricity and inclination driven by the outer companion that leads to a reduction in the misalignment. The outcome depends upon the ratio of the timescales of these effects. If the inner binary torque dominates, then the disk aligns to a polar orientation. If the outer companion torque dominates, then the disk undergoes KL oscillations. In that case, the highly eccentric and misaligned disk is disrupted and accreted by the inner binary, while some mass is transferred to the outer companion. However, when the torques are similar, the outer parts of the circumbinary disk can undergo large eccentricity oscillations while the inclination remains close to polar orientation. The range of initial disk inclinations that evolve to a polar orientation is smaller in the presence of the outer companion. Disk breaking is also more likely, at least temporarily, during the polar alignment process. The stellar orbits in HD 98800 have parameters such that polar alignment of the circumbinary disk is expected. In the absence of gas, solid particles are unstable at much smaller radii than the gas-disk inner tidal truncation radius because KL-driven eccentricity leads to close encounters with the binary.

*Unified Astronomy Thesaurus concepts:* Accretion (14); Stellar accretion disks (1579); Circumstellar disks (235); Protoplanetary disks (1300); Trinary stars (1714); Binary stars (154); Hydrodynamics (1963); Exoplanet formation (492); Planet formation (1241)

## 1. Introduction

Recent studies have investigated the dynamics of circumbinary disks that are initially misaligned with respect to the binary orbital plane (e.g., Facchini et al. 2013; Nixon et al. 2013; Aly et al. 2015; Martin & Lubow 2017; Lubow & Martin 2018; Cuello & Giuppone 2019; Zanazzi & Lai 2018; Smallwood et al. 2019, 2020). There are several observed cases of such disks. The quadruple star system HD 98800 consists of two binaries that orbit each other with a polar circumbinary gas disk around one of the binaries (Kennedy et al. 2019). In this work, we consider generally the effect of an outer companion (that is a binary in the case of HD 98800) on the dynamics of a highly misaligned circumbinary disk.

In a triple system composed of an inner binary with an outer companion in order for the stars to be in orbits that are stable against Kozai–Lidov (KL) oscillations of inclination and eccentricity (von Zeipel 1910; Kozai 1962; Lidov 1962; Naoz 2016; Hamers 2021), the orbit of the inner binary must be at an inclination of less than about 40° to the outer companion orbital plane. A polar circumbinary disk is inclined by 90° to the inner binary orbit and therefore must be at an inclination greater than about 50° to the outer companion orbit. If the inner binary were replaced by a single star, the outer

component would cause KL oscillations of such a highly misaligned disk (Martin et al. 2014; Fu et al. 2015a, 2015b). During these oscillations, the inclination and eccentricity of the disk are exchanged and the level of disk misalignment is reduced (Martin et al. 2016). The disk is able to respond globally provided that bending waves (which propagate at half the sound speed) can communicate the warp across the radial extent of the disk in less than the disk precession timescale. This occurs for thicker disks where the sound speed is sufficiently high (Papaloizou & Terquem 1995; Larwood et al. 1996). In order for the disk to remain in a polar configuration, it must be stabilized against KL oscillations. Stabilization is possible through the effects of the inner binary.

The inner binary drives nodal libration of test-particle orbits (Farago & Laskar 2010; Doolin & Blundell 2011; Naoz et al. 2017; Chen et al. 2019) meaning that a circumbinary disk undergoes nodal precession about the eccentricity vector of the inner binary. Dissipation within the disk leads to polar alignment, where the disk angular momentum is aligned with the binary eccentricity vector (Aly et al. 2015; Martin & Lubow 2017, 2018; Zanazzi & Lai 2018; Cuello & Giuppone 2019).

With both an inner binary and an outer companion, there are now two competing effects on the disk. Verrier & Evans (2009) examined this problem for test-particle orbits and found that particles close to the inner binary are stabilized against KL oscillations when the nodal libration period is shorter than the KL oscillation timescale.

In this work, for the first time, we examine the effect of an outer companion star on the evolution of a polar circumbinary disk. In Section 2 we begin by considering test-particle orbits. Particles that undergo KL oscillations are unstable and are ejected through close encounters with the inner binary. In Section 3 we present hydrodynamical gas-disk simulations. We find that the gas disk is stable much farther out than the particle orbits but the qualitative behavior of the disk is similar to a test particle if one of the torques dominates the other. However, when the inner binary and outer companion have similar magnitude effects, the disk can be both in a polar configuration and undergoing KL eccentricity oscillations. We consider some analytic estimates for the timescales in Section 4 and draw conclusions in Section 5.

## 2. Test-particle Dynamics

We examine test-particle orbits with analytic approximations and the $n$-body code REBOUND (Rein 2012) using the WHFast integrator. The inner binary has equal mass $M_{Aa} = M_{Ab} = 0.5\,M_A$, where the total mass is $M_A = M_{Aa} + M_{Ab}$. The inner binary orbit has semimajor axis $a_A$ and eccentricity $e_A$. The outer companion is treated as a single star with mass $M_B = M_A$ in a circular orbit with the inner binary with semimajor axis $a_{AB}$.

### 2.1. Inner Binary

First, we examine test-particle orbits around the inner binary without the outer companion. Tilt oscillations of a test particle on a nearly polar orbit at a distance $R$ from the inner binary, as a result of the nodal libration, occur with a period given by

$$t_{prec} = \frac{2\pi}{\omega_{prec}}, \qquad (1)$$

where

$$\omega_{prec} = k \frac{M_{Aa} M_{Ab}}{M_A^2} \left(\frac{a_A}{R}\right)^{7/2} \Omega_A, \qquad (2)$$

$$k = \frac{3\sqrt{5}}{4} e_A \sqrt{1 + 4e_A^2} \qquad (3)$$

(Farago & Laskar 2010; Lubow & Martin 2018), the angular frequency of the inner binary is $\Omega_A = 2\pi/P_A$, and the orbital period of the inner binary is $P_A$. The relation between the nodal libration period and distance is shown in the blue and red lines in the upper panel of Figure 1 for $a_A/a_{AB} = 0.5/15$ and $a_A/a_{AB} = 1.0/15$, respectively, both with $e_A = 0.5$. The separation is scaled by the separation of the outer companion, $a_{AB}$, and time by the orbital period of the outer companion, $P_{AB}$. Even though the outer companion does not affect $t_{prec}$, we do this for easier comparison later. The open square and open triangular points show the nodal libration period for test-particle orbits around the inner binary that are initially misaligned by $70°$. There is good agreement between the numerical simulations and the analytic approximation. The agreement gets better for larger $R/a_{AB}$ as expected because the quadrupole approximation used in deriving Equation (2) becomes more accurate. The agreement also gets better at a higher initial inclination where the orbit is closer to polar.

### 2.2. Outer Companion

With an outer companion, the timescale for KL oscillations of the test particle (replacing the inner binary by a single star of mass $M_A$) is given approximately by

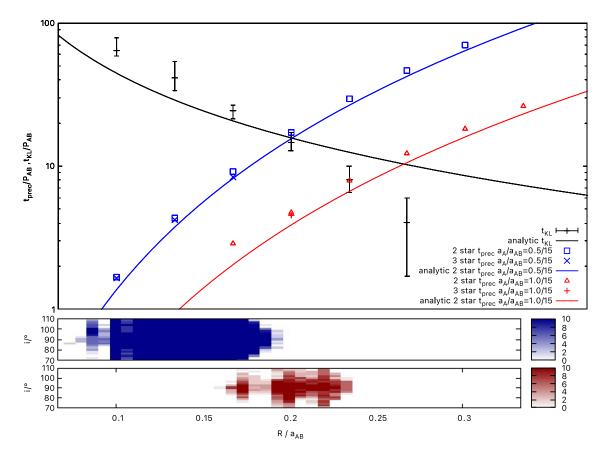$$t_{KL} = \frac{M_A + M_B}{M_B} \frac{P_{AB}^2}{P_p}(1 - e_{AB}^2) \qquad (4)$$

(Ford et al. 2000; Kiseleva et al. 1998), where $P_p = 2\pi / \sqrt{GM_A/R^3}$ is the orbital period of the test particle around the A star and $e_{AB}$ is the eccentricity of the outer companion orbit. We note that Equation (4) is derived under the quadrupole approximation in which the KL oscillation period for particles on initially circular orbits is formally infinite due to a logarithmic divergence (e.g., Lubow 2021). This equation gives an estimate for the period to within factors of order unity. The period $t_{KL}$ is plotted as a function of $R/a_{AB}$ by the black line in the upper panel of Figure 1. The black points show the KL oscillation periods obtained from test-particle simulations with an initial inclination of $70°$ in which the A binary is replaced by a single star. The KL period is very sensitive to the initial conditions and so we average the periods over 10 different values of the initial true anomaly. The higher the initial inclination, the better the agreement with Equation (4). For test particles that are at orbital radii $R/a_{AB} \gtrsim 0.2$, the analytic KL timescale is higher than the numerical value of the KL period. The analytic timescale is derived in the limit where the semimajor axis of the particle is much smaller than the binary semimajor axis.

### 2.3. Inner Binary and Outer Companion

We now consider test-particle simulations that include both the inner binary and the outer companion that orbit in the same orbital plane. The red crosses and blue $\times$'s in the upper panel of Figure 1 show the nodal libration periods for simulations that include the three stars. The libration period is not significantly altered by the outer star. However, the range of initial semimajor axes of the particle for which stable orbits exist is greatly reduced, as seen from the limited range in which the crosses and the $\times$'s appear in the plot.

The lower two panels show stability maps for test particles in the three star systems. The upper map is for $a_A/a_{AB} = 0.5/15$ and the lower map is for $a_A/a_{AB} = 1/15$. Each pixel is colored according to the number of stable cases among 10 simulations that have different (equally spaced) initial true anomaly values. We run each simulation for a time of $50,000\,P_A$ and define a particle to be unstable if its eccentricity becomes larger than 1, or its semimajor axis becomes large ($a_p > 10\,a_A$) or small ($a_p < a_A$) (see, for example, Quarles et al. 2018; Chen et al. 2020).

The stable region for test particles extends out to the radius where the numerically determined KL period becomes smaller than the nodal precession period. This was first seen by Verrier & Evans (2009) with regard to the HD 98800 system. Note that for the wider binary ($a_A/a_{AB} = 1/15$, lower panel), the outer edge is close to where the numerical KL period is equal to the nodal libration period while for the closer inner binary, the analytic KL timescale is a good approximation.

**Figure 1.** Test-particle orbits. Top panel: particle libration and KL timescales. The black line shows the KL timescale given by Equation (4). The blue and red lines show the nodal libration periods given by Equation (2) for $a_A/a_{AB} = 0.5/15$ and $a_A/a_{AB} = 1/15$, respectively. Each point shows a numerical test-particle simulation result. The error bars on the KL periods show the range of values with 10 different starting true anomaly values. The size of the error bars on the libration periods would be smaller than or equal to the size of the points. The lower panels show test-particle stability for a range of initial inclinations. Each pixel consists of 10 simulations that begin with different values of true anomaly.

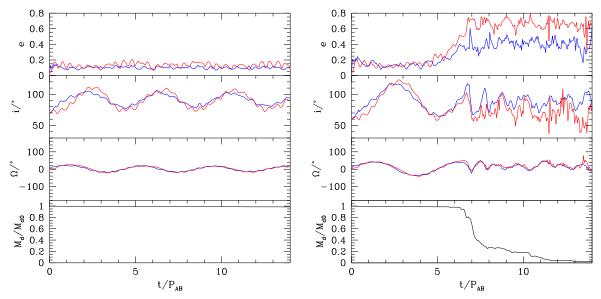## 3. Hydrodynamical Gas-disk Dynamics

We use the smoothed particle hydrodynamics (SPH) code PHANTOM (Price & Federrath 2010; Price et al. 2018) to model the evolution of a hydrodynamical gas disk with an inner binary and an outer companion. Misaligned disks in binaries have been widely studied with this code (e.g., Nixon et al. 2013; Nealon et al. 2018). We first consider the same triple star parameters as in Section 2. The accretion radii of the inner binary stars are $0.25\,a_A$ while the accretion radius of the outer companion star is $(0.25/15)a_{AB}$. Particles that move inside this radius are accreted, and their mass and angular momentum are added to the sink particle (Bate et al. 1995).

The disk has a mass of $0.001\,M_A$ with 500,000 particles initially. Because the disk mass is low, we ignore the self-gravity of the disk. The particles in the gas disk are initially distributed with a power-law surface density $\Sigma \propto R^{-3/2}$ between $R_{in} = 2\,a_A$ and $R_{out} = (1/3)a_{AB}$. The inner disk edge is chosen to be close to the tidal truncation radius from the inner binary. This is smaller around a polar binary compared to a coplanar binary (Lubow & Martin 2018; Franchini et al. 2019a). The outer disk edge is chosen to be close to the tidal truncation radius from the outer companion (Artymowicz & Lubow 1994). Note that an inclined disk has a larger tidal truncation radius than a coplanar disk (Lubow et al. 2015; Miranda & Lai 2015). The disk is locally isothermal with sound speed $c_s \propto R^{-3/4}$, and we take $H/R = 0.1$ at the initial disk

inner radius. This is chosen in order to make the shell-averaged smoothing length per scale height, $\langle h \rangle/H$, constant with radius (Lodato & Pringle 2007). The Shakura & Sunyaev (1973) viscosity $\alpha$ parameter is 0.01 and is implemented by adapting the SPH artificial viscosity with $\alpha_{AV} = 0.34$ (with $a_A/a_{AB} = 0.5/15$) or $\alpha_{AV} = 0.44$ (with $a_A/a_{AB} = 1/15$) and $\beta_{AV} = 2$ (Lodato & Price 2010). The disk is resolved with $\langle h \rangle/H = 0.29$ (with $a_A/a_{AB} = 0.5/15$) or $\langle h \rangle/H = 0.23$ (with $a_A/a_{AB} = 1/15$). As $H/R \gg \alpha$, disk warping occurs in the bending wave regime (Papaloizou & Pringle 1983). We bin the particles into 100 bins in spherical radius and average the properties of the particles in each bin. The inclination and the longitude of ascending node are calculated in a frame relative to the inner binary (see Equations (1) and (3) in Chen et al. 2019).
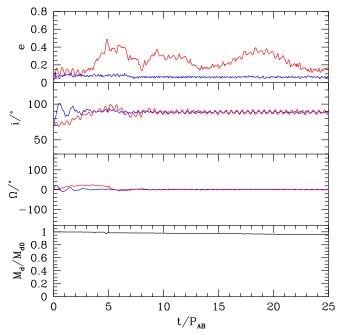
### 3.1. Wide Inner Binary

We first consider simulations with a relatively large ratio of the binary semimajor axes, $a_A/a_{AB}$, so that the disk is radially narrow. The left panel of Figure 2 shows the evolution of a disk around a binary with $a_A/a_{AB} = 1/15$ and $e_A = 0.5$ that is initially at an inclination of $70°$ to the binary orbit. The disk undergoes tilt oscillations and aligns toward a polar inclination. The behavior at the two radii in the disk that are plotted is similar which indicates that there is little warping in the disk. This is a natural consequence of being in the bending wave

**Figure 2.** Hydrodynamical gas-disk simulations for the wide inner binary with $a_A/a_{AB} = 1/15$ and $e_A = 0.5$ with initial disk inclinations of $70°$ (left) and $60°$ (right). The blue lines show the inner disk at $R = 2\,a_A$, and the red lines show the outer disk at $R = (1/3)a_{AB}$. The time is in units of the orbital period of the outer companion. From top to bottom, the panels show the disk eccentricity, inclination, longitude of ascending node, and the circumbinary disk mass.

regime. The communication timescale, $t_c \sim 2R/c_s \sim 2(H/R)^{-1}/\Omega_{out}$, where $\Omega_{out}$ is the Keplerian frequency in the outer parts of the disk, is roughly $0.9\,P_{AB}$. Because the tilt oscillations seen in the left panel of Figure 2 occur over longer timescales, the disk behaves rigidly with little warping. There is also little disk eccentricity growth in this simulation as the inner binary torque is dominating the outer companion torque and suppressing the KL oscillations. The parameters of the inner binary and disk are exactly the same as those in the simulation presented in Martin & Lubow (2017) except that the initial disk inclination here is $70°$, compared to $60°$ in Martin & Lubow (2017). The behavior is qualitatively very similar except that the tilt oscillations occur on a shorter timescale.

The right-hand panel of Figure 2 shows a simulation with the same parameters as the left panel but a lower inclination of $60°$. At a lower inclination, the nodal libration period is longer. The parameters are exactly those presented in Martin & Lubow (2017) in which the disk is aligned to polar without the outer companion star. Initially, the disk undergoes tilt oscillations with a reduced period in the presence of the outer companion. The period of the first oscillation is about $4.75\,P_{AB} \approx 200\,P_A$ with the outer companion, while it was about $250\,P_A$ without the outer companion (see Figure 1 in Martin & Lubow 2017). The test-particle nodal libration timescale is not significantly affected by the companion star (see Section 2) and so this is likely because the disk is able to spread out to larger radii without the outer companion (see also e.g. Ronco et al. 2021). The libration period for a rigid disk is set by an appropriate average of the precession periods over the disk radial extent. However, after just one libration period, the KL effect from the companion dominates the dynamics and the disk becomes highly eccentric. The eccentricity growth is uniform over the disk radial extent. This leads to a strong interaction with the inner binary that largely disrupts the disk. Some of the disk material is transferred to the outer companion (Franchini et al. 2019b), and it ends up with a more massive disk than the inner binary. At a time of $14\,P_{AB}$, the inner binary has accreted 73% of the initial disk mass and the remaining circumbinary disk
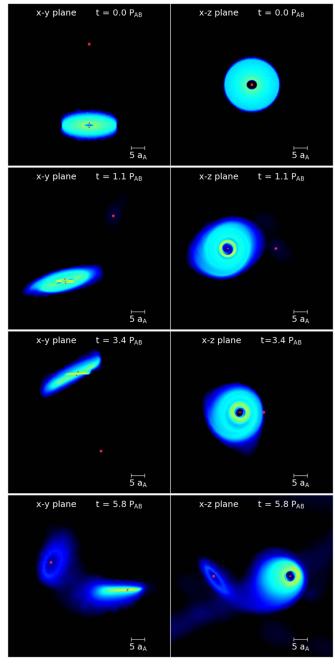


**Figure 3.** Same as the left panel of Figure 2 except for $a_A/a_{AB} = 0.5/15$.

contains about 2%. The companion has accreted about 6% and the disk left around it contains about 10%. The remaining 9% of the material either has been flung out to a large radius or is forming a circumtriple disk. The range of initial inclinations that lead to polar alignment is smaller in the presence of an exterior binary companion.

### 3.2. Close Inner Binary

Figure 3 shows a simulation with a smaller inner binary separation of $a_A/a_{AB} = 0.5/15$ and $e_A = 0.5$ with an initial disk inclination of $70°$. The initial disk configuration is shown in the top panels of Figure 4. The tilt oscillation period is shorter for this closer binary, and the inner parts of the disk undergo rapid polar alignment. The disk is strongly warped by a time of about

**Figure 4.** Close inner binary simulation with $a_A/a_{AB} = 0.5/15$ and $e_A = 0.5$ at times of $t = 0$, 1.1, 3.4, and 6 $P_{AB}$ from top to bottom. The red circles show the three stars scaled to the size of their sink radius. The left panels show the $x-y$ plane in which both the inner binary and the outer companion orbit. The right panels show the $x-z$ plane. In the final time, the circumbinary disk is perpendicular to the inner binary and the outer companion orbits. The highly eccentric outer parts of the circumbinary disk have transferred material to the outer companion, and it has a low-mass disk.

1 $P_{AB}$, where there is about a 20° difference over a radial range of 0.03 $a_{AB}$ in both the inclination and the nodal phase angles (see the second row of Figure 4). The warp strength then weakens, and the warp location propagates outwards in time (see the third row of Figure 4). Note that with higher-resolution simulations, the disk may look more cleanly broken rather than warped (Nealon et al. 2015). We see slower polar alignment in the outer parts of the disk compared to the inner disk. However, the outer parts of the disk undergo significant eccentricity
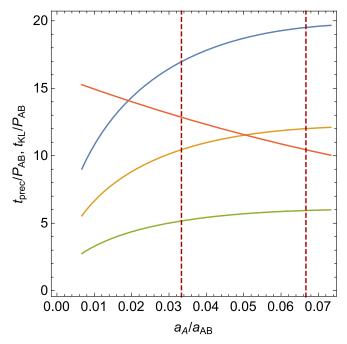
growth as a result of the KL effect. The eccentricity growth is not uniform with radius but increases with separation from the inner binary. These eccentricity oscillations of the polar disk may be long-lived because the disk remains in a polar configuration, that is, above the critical inclination required for KL disk oscillations (Lubow & Ogilvie 2017; Zanazzi & Lai 2017). Long-lived KL disk oscillations have been seen before when there is a source of high-inclination material feeding the formation of circumstellar disks (Smallwood et al. 2021). The lower panels of Figure 4 show the disk at a time of $t = 5.8 P_{AB}$, near the peak disk eccentricity. The circumbinary disk is polar to both the inner binary and the outer companion orbit while being quite eccentric. A low-mass disk can be seen around the companion that has formed as a result of mass transfer during the high-eccentricity disk phase (e.g., Franchini et al. 2019b).

## 4. Global Disk Timescales

We now estimate analytically the global disk libration period (in the absence of the outer companion) and the KL timescale (in which we replace the inner binary with a single star). The global precession rate is determined by the precessional torque on the disk divided by its angular momentum, assuming that the disk does not break and behaves rigidly (Papaloizou & Terquem 1995; Larwood & Papaloizou 1997; Lubow & Ogilvie 2001). This is expected in the bending wave regime when the communication timescale is shorter than the global precession timescale. We use Equation (16) in Lubow & Martin (2018) to calculate the global disk precession period due to the inner binary and Equation (4) in Martin et al. (2014) to calculate the global disk KL timescale due to the outer companion. Note that there is no inclination dependence in these estimates, and they are valid close to polar. We assume a power-law surface density profile distributed between $R_{in} = 2.3 \, a_A$ and $R_{out} = (5.5/15)a_{AB}$. While the inner edge of a polar circumbinary disk is smaller than this value of $R_{in}$ (Franchini et al. 2019a), the surface density profile tapers close to the binary. We choose this value because it is close to the peak in the surface density profile in our simulations.

Figure 5 shows these timescales as a function of the ratio of the binary semimajor axes. In our wide binary simulations with $a_A/a_{AB} = 1/15$, the libration period is about 4.75 $P_{AB}$, in rough agreement with this analytic estimate for $e_A = 0.5$ (green line). The KL timescale decreases with increasing inner binary separation only because the disk inner radius becomes larger. These analytic timescales provide an estimate of the outcome of a disk simulation if the disk is in good radial communication (when the communication timescale is shorter than the global precession timescale). If the global disk KL timescale is shorter than the global disk nodal libration period, then the disk does not remain polar. It undergoes KL oscillations and may be accreted onto the inner binary and transferred to the companion. However, if the nodal libration period is shorter than the KL timescale, then we expect the disk to move to polar alignment.

We also considered some simulations with lower binary eccentricity. For the wide inner binary ($a_A/a_{AB} = 1/15$), with $e_A = 0.2$ and 0.3, the disk is destroyed through KL oscillations. This is in agreement with the analytic prediction in Figure 5. For the close binary simulation ($a_A/a_{AB} = 0.5/15$), we found for $e_A = 0.2$ and 0.3 that the disk breaks and much of the material ends up in a polar configuration. When the disk

**Figure 5.** Analytic estimates for the global precession period around a binary with eccentricity $e_A = 0.2$ (blue line), 0.3 (yellow line), and 0.5 (green line) and the KL oscillation timescale (red line) for a disk with $\Sigma \propto R^{-3/2}$ from $R_{in} = 2.3\, a_A$ out to $(1/3)a_{AB}$. The vertical dashed lines show the values of the semimajor axis ratios used in the SPH simulations ("close inner binary" on the left and "wide inner binary" on the right).

breaks, the inner ring quickly aligns to polar, while the outer ring undergoes KL oscillations and is disrupted when the disk becomes highly eccentric. The outer ring is accreted onto the stars and forms a disk around the third star. The inner polar ring then spreads outwards, and the long-term behavior is similar to that shown in Figure 3. Therefore, disk breaking in a radially wide disk can affect the outcome and help to stabilize the disk against KL oscillations.

## 5. Conclusions

A polar circumbinary disk that has an outer companion is subject to two competing dynamical effects. The inner binary causes nodal libration and polar alignment. The outer companion drives KL oscillations that lead to coplanar alignment. The outcome depends strongly upon the inner binary eccentricity, the initial disk inclination, and the ratio of the binary semimajor axes. If the global nodal libration period is shorter than the global KL timescale, the disk moves toward polar alignment. If the KL timescale is shorter than the nodal libration period, the disk becomes highly eccentric and is largely destroyed, either being accreted onto the central binary or forming a disk around the companion. If the timescales are similar, an outer companion to a polar circumbinary gas disk can cause the eccentricity growth of the disk while the disk inclination remains in a polar configuration. The range of initial inclinations that lead to a polar-aligned disk is reduced by the outer companion and disk breaking is more likely, at least temporarily.

The outermost stable particle orbit is significantly closer in than the outer edge of a gas disk. Thus, a polar gas disk can extend to much larger radius than a particle disk. Solid bodies may be on stable polar orbits while the gas disk is present, but

once the gas has dissipated, they may be unstable to KL oscillations and become ejected from the system.

For the HD 98800 system, the ratio of semimajor axes is $a_A/a_{AB} = 0.02$, and the eccentricity of the inner binary is 0.79. Polar alignment is then expected (see Figure 5). The eccentricity of the outer companion orbit is also relatively large at around 0.52. The high eccentricity of the outer companion leads to a smaller outer truncation radius for the circumbinary disk (Artymowicz & Lubow 1994). For a power-law disk density distribution in radius, the effective radius for the disk precession scales approximately with the periastron separation, $R_{eff} \propto (1 - e_{AB})$. For fixed stellar masses and outer companion orbital period, the disk KL timescale varies with $(1 - e_{AB}^2)^{3/2}/R_{eff}^{3/2} \propto (1 + e_{AB})^{3/2}$ (see Equation (4)). Therefore, a higher outer companion eccentricity leads to a longer disk KL oscillation timescale and polar alignment is more likely.

### ORCID iDs

Rebecca G. Martin ⓘ https://orcid.org/0000-0003-2401-7168
Stephen Lepp ⓘ https://orcid.org/0000-0003-2270-1310
Stephen H. Lubow ⓘ https://orcid.org/0000-0002-4636-7348
Matthew A. Kenworthy ⓘ https://orcid.org/0000-0002-7064-8270

### References

Aly, H., Dehnen, W., Nixon, C., & King, A. 2015, MNRAS, 449, 65
Artymowicz, P., & Lubow, S. H. 1994, ApJ, 421, 651
Bate, M. R., Bonnell, I. A., & Price, N. M. 1995, MNRAS, 277, 362
Chen, C., Franchini, A., Lubow, S. H., & Martin, R. G. 2019, MNRAS, 490, 5634
Chen, C., Lubow, S. H., & Martin, R. G. 2020, MNRAS, 494, 4645
Cuello, N., & Giuppone, C. A. 2019, A&A, 628, A119
Doolin, S., & Blundell, K. M. 2011, MNRAS, 418, 2656
Facchini, S., Lodato, G., & Price, D. J. 2013, MNRAS, 433, 2142
Farago, F., & Laskar, J. 2010, MNRAS, 401, 1189
Ford, E. B., Kozinsky, B., & Rasio, F. A. 2000, ApJ, 535, 385
Franchini, A., Lubow, S. H., & Martin, R. G. 2019a, ApJL, 880, L18
Franchini, A., Martin, R. G., & Lubow, S. H. 2019b, MNRAS, 485, 315
Fu, W., Lubow, S. H., & Martin, R. G. 2015a, ApJ, 807, 75
Fu, W., Lubow, S. H., & Martin, R. G. 2015b, ApJ, 813, 105
Hamers, A. S. 2021, MNRAS, 500, 3481
Kennedy, G. M., Matrà, L., Facchini, S., et al. 2019, NatAs, 3, 230
Kiseleva, L. G., Eggleton, P. P., & Mikkola, S. 1998, MNRAS, 300, 292
Kozai, Y. 1962, AJ, 67, 591
Larwood, J. D., Nelson, R. P., Papaloizou, J. C. B., & Terquem, C. 1996, MNRAS, 282, 597
Larwood, J. D., & Papaloizou, J. C. B. 1997, MNRAS, 285, 288
Lidov, M. L. 1962, P&SS, 9, 719
Lodato, G., & Price, D. J. 2010, MNRAS, 405, 1212
Lodato, G., & Pringle, J. E. 2007, MNRAS, 381, 1287
Lubow, S. H. 2021, MNRAS, 507, 367
Lubow, S. H., & Martin, R. G. 2018, MNRAS, 473, 3733
Lubow, S. H., Martin, R. G., & Nixon, C. 2015, ApJ, 800, 96
Lubow, S. H., & Ogilvie, G. I. 2001, ApJ, 560, 997
Lubow, S. H., & Ogilvie, G. I. 2017, MNRAS, 469, 4292
Martin, R. G., & Lubow, S. H. 2017, ApJL, 835, L28
Martin, R. G., & Lubow, S. H. 2018, MNRAS, 479, 1297

Martin, R. G., Lubow, S. H., Nixon, C., & Armitage, P. J. 2016, MNRAS, 458, 4345
Martin, R. G., Nixon, C., Armitage, P. J., Lubow, S. H., & Price, D. J. 2014, ApJL, 790, L34
Miranda, R., & Lai, D. 2015, MNRAS, 452, 2396
Naoz, S. 2016, ARA&A, 54, 441
Naoz, S., Li, G., Zanardi, M., de Elía, G. C., & Di Sisto, R. P. 2017, AJ, 154, 18
Nealon, R., Dipierro, G., Alexander, R., Martin, R. G., & Nixon, C. 2018, MNRAS, 481, 20
Nealon, R., Price, D. J., & Nixon, C. J. 2015, MNRAS, 448, 1526
Nixon, C., King, A., & Price, D. 2013, MNRAS, 434, 1946
Papaloizou, J. C. B., & Pringle, J. E. 1983, MNRAS, 202, 1181
Papaloizou, J. C. B., & Terquem, C. 1995, MNRAS, 274, 987
Price, D. J. 2007, PASA, 24, 159

Price, D. J., & Federrath, C. 2010, MNRAS, 406, 1659
Price, D. J., Wurster, J., Tricco, T. S., et al. 2018, PASA, 35, e031
Quarles, B., Satyal, S., Kostov, V., Kaib, N., & Haghighipour, N. 2018, ApJ, 856, 150
Rein, H. 2012, MNRAS, 427, L21
Ronco, M. P., Guilera, O. M., Cuadra, J., et al. 2021, ApJ, 916, 113
Shakura, N. I., & Sunyaev, R. A. 1973, A&A, 24, 337
Smallwood, J. L., Franchini, A., Chen, C., et al. 2020, MNRAS, 494, 487
Smallwood, J. L., Lubow, S. H., Franchini, A., & Martin, R. G. 2019, MNRAS, 486, 2919
Smallwood, J. L., Martin, R. G., & Lubow, S. H. 2021, ApJL, 907, L14
Verrier, P. E., & Evans, N. W. 2009, MNRAS, 394, 1721
von Zeipel, H. 1910, AN, 183, 345
Zanazzi, J. J., & Lai, D. 2017, MNRAS, 467, 1957
Zanazzi, J. J., & Lai, D. 2018, MNRAS, 473, 603